Results in Engineering 20 (2023) 101465

Contents lists available at ScienceDirect

Results in Engineering

journal homepage: www.sciencedirect.com/journal/results-in-engineering

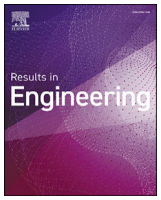

Research paper

Fractional viscoelastic models for the estimation of the frequency response of rubber bushings based on relaxation tests

Jose Calaf-Chica [a,*], Víctor Cea-González [a], María-José García-Tárrago [b], Francisco-Javier Gómez-Gil [b]

[a] Research Group CIMa; University of Burgos, Avenida Cantabria s/n, Burgos, 09006, Spain
[b] Department of Electromechanical Engineering; University of Burgos, Avenida Cantabria s/n, Burgos, 09006, Spain

ARTICLE INFO

Keywords:
Viscoelasticity
Rubber bushing
Loss factor
Dynamic stiffness
Fractional derivative

ABSTRACT

Estimation of the viscoelastic properties of rubber bushings at very high frequencies (up to 2 kHz) is a challenge for many damping component manufacturers in the design stage of a quality monitoring procedure. This investigation is focused on the capability of lower strain rate testing procedures, such as relaxation tests, to estimate and extrapolate the dynamic behavior of rubber bushings from low to moderate frequencies. Fractional Zener models are employed to approach bushing behavior in experimental relaxation tests, thus leading to a linear viscoelastic model which is employed to estimate the dynamic behavior of rubber bushing under harmonics loads up to 150 Hz. The validation of this extrapolation procedure is performed by comparing these analytical results with experimental dynamic harmonic tests applied to the same rubber bushings. The deviation between both curves demonstrates that it is difficult to compare the behavior from very small deformation rates (relaxation tests) to higher deformation rates (harmonic dynamic tests) due to the nonlinear behavior of the rubber and its amplitude dependence. However, this investigation demonstrates that the relaxation tests contain enough data to define the frequency behavior of linear viscoelastic materials up to moderate frequencies.

Symbols & abbreviations

BEV: battery electric vehicle
DMA: dynamic mechanical analyzer
FCEV: fuel cell electric vehicle
MSE: mean square error
RCB: rubber-compound bushing
α: fractional order of a springpot
c: damping coefficient
δ: displacement
F: load
f: frequency
$\hat{f}$: cutoff frequency
Γ: Gamma function
k: spring coefficient
k^*: complex dynamic stiffness
k': storage stiffness
k'': loss stiffness
m: linear coefficient of a springpot
N: time discretization
LF: loss factor
ψ: phase angle
t: time

1. Introduction

Comfort is a crucial objective in any automotive design. The drive train, motor, and engine transmit noise and vibration into the chassis. These uncomfortable feelings also include the vibrations transmitted from the road surface [1] or the brake system [2–4]. In that sense, vibroacoustic modeling is an essential subject that any automotive designer must treat [5,6]. New drive concepts have recently grown in electric mobility with massive innovative projects around hydrogen as an energy vector [7–9]. As viable solutions for decarbonization, battery electric vehicles (BEVs) have the limitations of running time and reloading time of the battery. This limitation is solved by the alternative of fuel cell electric vehicles (FCEVs). FCEVs use energy stored as hydrogen, replacing the battery system used in BEVs. The rest of the vehicle

* Corresponding author.
E-mail address: jcalaf@ubu.es (J. Calaf-Chica).

https://doi.org/10.1016/j.rineng.2023.101465
Received 27 July 2023; Received in revised form 21 September 2023; Accepted 26 September 2023
Available online 2 October 2023
2590-1230/© 2023 The Author(s). Published by Elsevier B.V. This is an open access article under the CC BY-NC-ND license (http://creativecommons.org/licenses/by-nc-nd/4.0/).

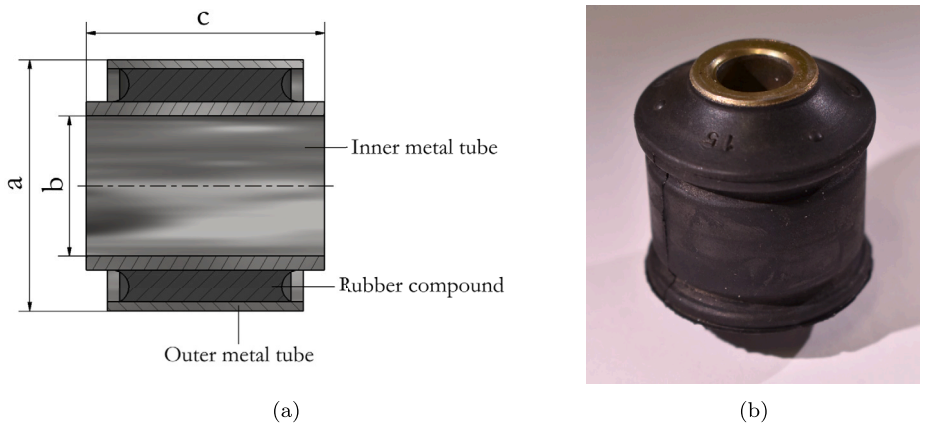

Fig. 1. (a) Schematic representation and (b) a basic rubber bushing for vibration-isolation manufactured by CMP Automotive company.

is similar to a BEV set-up, using an electric motor as a power system [10]. The expanding scenario of BEVs and FCEVs in future trends in the automotive sector generates new challenges in vibroacoustic modeling with noise and vibration at higher frequencies [11].

Internal combustion engine vehicles generate vibration and noise in a frequency range of up to 200 Hz [12]. In electric cars, this upper limit grows up to 2-3 kHz [13]. This fact is the origin of the challenge in vibroacoustic modeling because the damping capabilities of any assembly are strongly affected at these high frequencies [14,15]. Automotive suppliers that provide innovative solutions for a smooth and comfortable ride must provide spare parts for a range of light and commercial vehicles in a growing scenario of power alternatives for mobility. The use of rubber bushings is an effective way of reducing the vibration and shock between different parts of the vehicle [16]. These rubber vibration-isolating mounts separate rigid parts, reducing vibration and noise by absorbing and damping the kinetic energy transmitted from part to part [17]. These elements are commonly used in different mechanical joints: road suspensions, engine or electric motor mounting, pivot arms, etc. Rubber bushings are usually composed of outer and inner metallic tubes connected by a vulcanized and bonded rubber compound (see Fig. 1). This basic geometry concept is extended to more complex set-ups in order to optimize and provide specific stiffness and damping characteristics in different directions [18]. In addition, these parts are designed to show the optimal behavior in the frequency range where vibrations are transmitted between the joint components. As a consequence, the design of rubber bushings for an electric motor or a combustion engine significantly differs as a result of the frequency range of each power system [19].

Rubber compounds, commonly used in the design process of vibration-isolation bushings [20–22], are soft materials whose response is in a spectrum between elastic and Newtonian fluid behaviors. Referred to as viscoelastic materials, these compounds are capable of transmitting a load between the outer and inner tubes and, at the same time, dissipating a fraction of the mechanical work [23]. Characterizing and understanding the mechanical response of rubber-compound bushings (RCB) are critical for the automotive suppliers of these parts. There are three testing procedures [24] to quantify the viscoelastic response of an RCB (see Fig. 2): (i) relaxation tests, where the part is subjected to a constant displacement, registering the load response; (ii) creep tests, where the part is subjected to a constant load, registering the displacement response; and (iii) dynamic mechanical tests, where oscillatory or harmonic displacement is applied, registering the load response. The last one is performed in DMAs (dynamic mechanical analyzers) for materials with solid behavior and rheometers in the case of liquid-like materials. The choice of the test method depends on the application in which the sample or component is to be used. In the specific case of elastomeric materials employed for noise and vibration dissipation, testing in DMAs is the most common practice [25]. However, there is a limitation in available providers of DMA machines for testing at very high frequencies. Furthermore, testing rubber bushings requires load amplitudes beyond the limits of these DMAs. There are dynamic testing machines focused on this specific issue, but the market of high-frequency dynamic stiffness test rigs for elastomeric mounts is too limited to consider alternatives in order to extrapolate the high-frequency response with experimental tests performed at lower frequencies.

The aim of this investigation is to demonstrate the capability of lower-frequency testing procedures in order to extrapolate viscoelastic behavior at higher frequencies. Therefore, firstly, experimental relaxation tests are carried out to design the extrapolation procedure of viscoelastic properties at low to moderate frequencies (from 5 Hz to 150 Hz). Next, experimental harmonic tests are also performed to validate this methodology.

This paper has been organized into three main sections: (i) a description of the viscoelastic numerical model used to approach experimental relaxation curves of RCBs; (ii) an overview of the numerical method employ to solve for the fractional Maxwell-Wiechert constitutive equation and (iii), the experimental validation of the estimated viscoelastic models through dynamic tests of the RCBs at a range from low to moderate frequencies.

2. Methodology

As previously described, this investigation aim to use relaxation tests in RCBs to extrapolate their behavior at low to moderate frequencies under dynamic harmonic excitations. Fig. 3 shows a diagram of the extrapolation procedure. Blue rectangles represent the experimental tests and grey rectangles show the analytical procedures. Solid-lined rectangles state testing procedures (analytical or experimental), and dashed-lined rectangles represent data or property that has been estimated or registered. The extrapolation procedure begins with the load and displacement experimental data obtained from relaxation tests of RCB. The coefficients of a viscoelastic model are established from an iterative process that seeks to simulate the load versus displacement data obtained from the experimental relaxation tests. Next, the estimated viscoelastic model is used to simulate a dynamic harmonic test in a frequency range from 5 to 150 Hz. The simulated dynamic stiffness is the ratio between an input harmonic load signal and the harmonic displacement obtained from the previously estimated viscoelastic model. On the other hand, experimental dynamic harmonic tests are performed in a similar frequency range for the same RCBs. Finally, both dynamic stiffnesses, the one obtained experimentally and the one estimated with the extrapolation procedure, are compared.

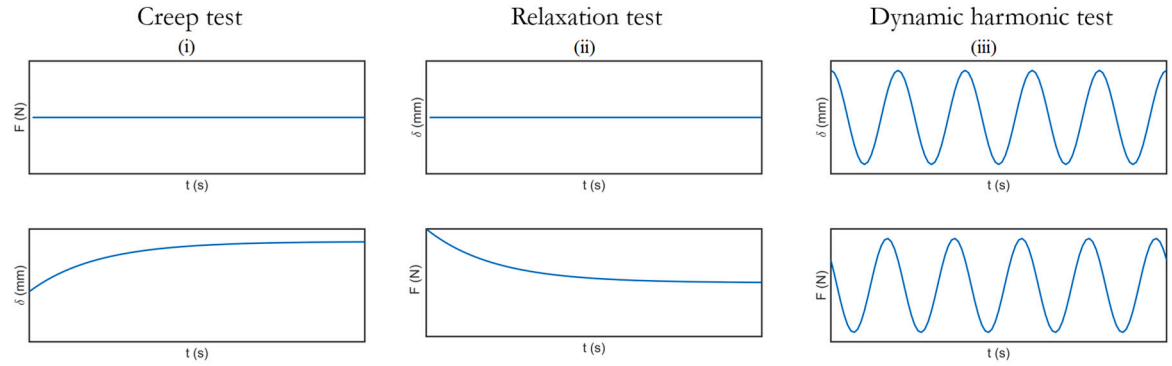

Fig. 2. Testing procedures for viscoelastic characterization of materials (F: load; δ: displacement; t: time): (i) creep test, (ii) relaxation test and (iii) dynamic harmonic test.

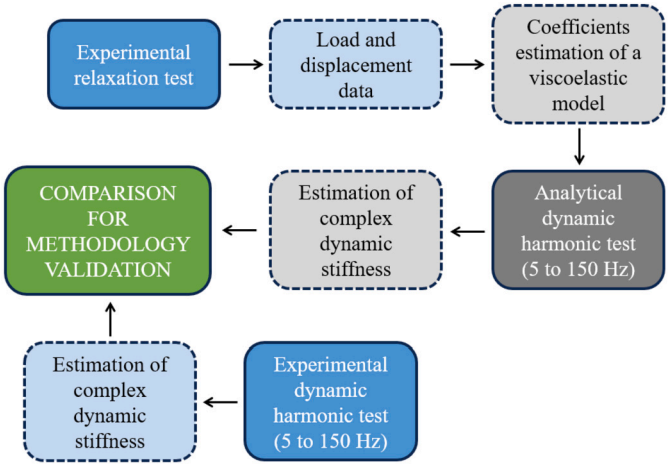

Fig. 3. Diagram of validation of the extrapolation process in which the dynamic frequency response of RCBs is extrapolated from the relaxation tests.

The selection of an appropriate viscoelastic model is the most critical step in this extrapolation procedure. For that reason, a brief introduction to the most common viscoelastic models has been included in this methodology to justify the eventually chosen one.

When a viscoelastic material is subjected to a harmonic displacement $\delta = \delta_0 e^{i2\pi f t}$, the registered load shows the same frequency f but with a difference ψ in the phase angle, $F = F_0 e^{i(2\pi f t+\psi)}$. This difference $\psi(f)$ is directly related to the damping capability of the material and its value depends on the frequency f. Therefore, the complex dynamic stiffness, which is the ratio of the registered load to the applied harmonic displacement, gives a measurement of the viscoelastic response of an RCB to a sinusoidal displacement [26]. The real component of complex dynamic stiffness, named storage stiffness, represents the elastic and recoverable energy, while the imaginary component of complex dynamic stiffness, named loss stiffness, represents the dissipated energy of the pure viscous behavior [27]. Moreover, the loss factor (LF) is the ratio between the loss stiffness and the storage stiffness. The most important properties estimated from the registered data of a dynamic harmonic test in an RCB are: (i) the absolute value of the complex stiffness ($|k^*(f)|$), and (ii), the loss factor (LF) which is also the tangent of the phase between the registered load and the applied harmonic displacement at the excitation frequency.

The linear theory of viscoelasticity provides powerful mathematical tools to predict the mechanical response of a material or part during an arbitrary displacement spectrum. The mathematical models used to simulate the viscoelastic behavior are based, in a conventional approach, on two basic elements: the Hookean spring and the Newtonian dashpot. The Hookean spring is represented by equation (1):

$$F(t) = k\delta(t) \tag{1}$$

while the Newtonian dashpot is governed by the following equation (2):

$$F(t) = c\dot{\delta}(t) \tag{2}$$

The combination of these two elements in series or parallel provides more complex behavior and, depending on the evaluated material, each model will be more or less appropriate. Fig. 4 shows the characteristics of three conventional viscoelastic material models, their constitutive equations and their response to harmonic excitation, in terms of the absolute value of the dynamic stiffness ($|k^*|$) and the loss factor (LF) [28].

The equations in Fig. 4 corresponding to the absolute value of the dynamic stiffness ($|k^*|$) and the loss factor (LF) of these three conventional models (Maxwell, Kelvin-Voigt, and Zener models) are implemented in Matlab® and results are compared in Fig. 5. The coefficients used for this comparison were: $k_0 = k_1 = k = 1000$ N/mm and $c = c_1 = 1000$ N.s/mm. Fig. 5 shows that the Maxwell and Kelvin-Voigt models show a frequency dependency of the LF similar to a power function, with a monotone decrease in the case of the Maxwell model and a monotone increase in the case of the Kelvin-Voigt model. In contrast, the dynamic stiffness of the Maxwell model $|k^*|$ shows a frequency dependency similar to a power function until reaching a specific value of the frequency, $\hat{f} = \frac{k}{2\pi c}$ named as cutoff frequency, where monotone increase finishes in the specific value of the spring k. In the case of the Kelvin-Voigt model, there is an opposite behavior: a constant value of $|k^*| = k$ up to the proximity of $\hat{f}$ and, after that, a monotone increase with a power function with the same power coefficient as the Maxwell model.

Zener model shows, as an approach, a combined behavior of the Maxwell and Kelvin-Voigt models. LF shows the same behavior as the Kelvin-Voigt model until approaching the cutoff frequency $\hat{f}$, where power dependency changes until reaching the power of the Maxwell model. In this viscoelastic model, $|k^*|$ is limited to a range between k_0 and $k_0 + k_1$, centering the transition between these two values in the proximity of the cutoff frequency.

Fig. 5 shows with double arrows how the coefficients of each viscoelastic model modify the curves that relate $|k^*|$ and LF to the frequency f. The color of each arrow indicates the curve to which it is related. The symbol or symbols near each arrow indicate the coefficient that generates the specific change in the curve. Finally, the double arrow indicates the direction of the translation produced by each change. In Fig. 5b, there is a specific symbol (a filled circle) that indicates no changes in the curve. In the case of $|k^*|$ of the conventional Zener model, k's coefficients near the horizontal lines indicate the coefficients that affect the vertical position of each horizontal line. The alteration of any coefficient in the Maxwell and Kelvin-Voigt models only generates the translation of the curves in a log-log representation. Zener

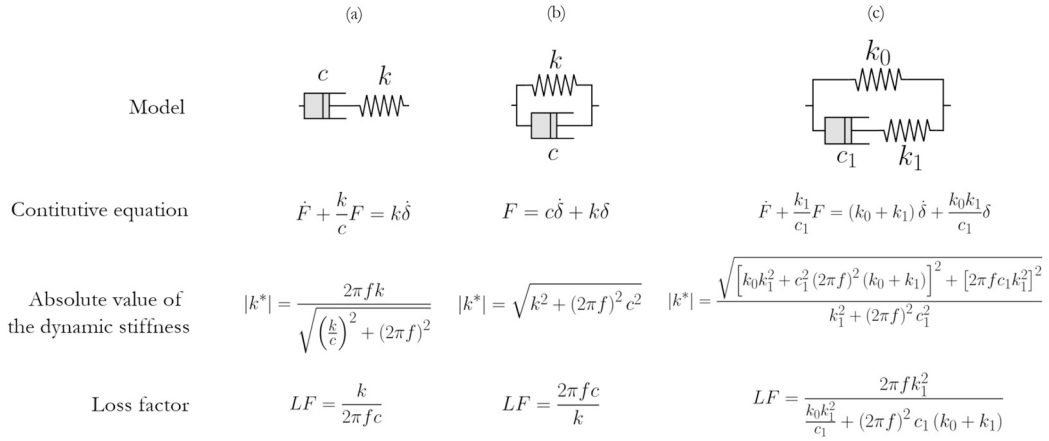

Fig. 4. Conventional viscoelastic models: (a) Maxwell model, (b) Kelvin-Voigt model, and (c) Zener model [28].

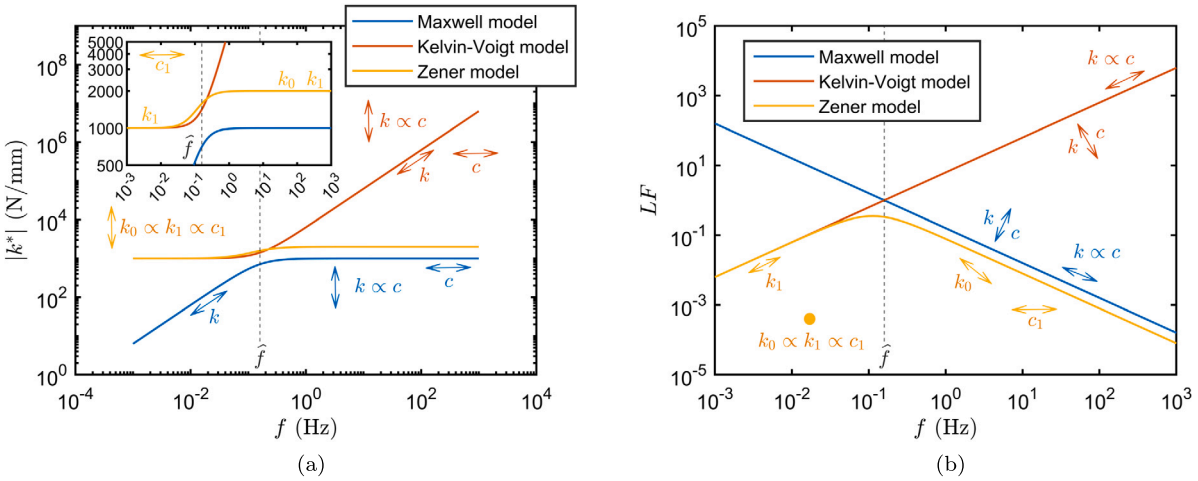

Fig. 5. Comparison of the mechanical response of a Maxwell model (k = 1000 N/mm; c = 1000 N.s/mm), a Kelvin-Voigt model (k = 1000 N/mm; c = 1000 N.s/mm), and a Zener model (k_0 = 1000 N/mm; k_1 = 1000 N/mm; c_1 = 1000 N.s/mm); (a) absolute value of the dynamic stiffness, and (b) loss factor according to the formulation presented in Fig. 4.

model shows a similar behavior, except for $|k^*|$ where a change in k's coefficients modulates the vertical position of the horizontal lines, with no significant changes in the first derivatives used to connect the two horizontal levels. A proportional change of all the coefficients of the evaluated models ($k \propto c$ in the case of Maxwell and Kelvin-Voigt models and $k_0 \propto k_1 \propto c_1$ in the case of the Zener model) generates a vertical translation of the curves in the case of $|k^*|$ and no changes in the case of LF. Although the conventional Zener model is the one that best represents the viscoelastic behavior, it presents significant limitations in approaching a real viscoelastic material in the frequency domain, because the scaling of the curves in a specific direction in a log-log representation is clearly limited. To overcome these weaknesses, a combination of Maxwell models can be connected in parallel to the Zener model, thus leading to the Maxwell-Wiechert model [29]. Each new Maxwell branch generates a new cutoff frequency, in the representation of $|k^*|$ and LF, with new k steps in the case of $|k^*|$, and new peaks in the case of LF at each new cutoff frequency. In addition, the use of more sophisticated elements, such as springpot elements, allows for representing the frequency dependence of the viscoelastic material with more flexibility and a minimum number of parameters [30–32].

Springpot elements are linear elements that use fractional derivatives in their constitutive equation (see equation (3)), with two coefficients that define their behavior: m is a linear coefficient, and α is the fractional order of the derivative with a value between 0 and 1. This element is commonly used to substitute the dashpot elements of the previously analyzed models. Thus, their constitutive equations change to those included in Equation (4). These equations must be solved by numerical methods, such as the one based on the Grünwald-Letnikov fractional derivative [33–35], which is obtained from the derivative definition (see Equation (5)).

$$F = mD^{\alpha}[\delta] \tag{3}$$

Fractional Maxwell model: $D^{\alpha}[F]+\frac{k}{m}F=kD^{\alpha}[\delta]$

Fractional Kelvin-Voigt model: $F=mD^{\alpha}[\delta]+k\delta$

Fractional Zener model: $D^{\alpha}[F]+\frac{k_1}{m_1}F=\left(k_0+k_1\right)D^{\alpha}[\delta]+\frac{k_0k_1}{m_1}\delta$

(4)

$$D^{\alpha}[f]=\lim_{N\to\infty}(\Delta t)^{-\alpha}\sum_{j=0}^{N-1}\frac{\Gamma(j-\alpha)}{\Gamma(-\alpha)\Gamma(j+1)}f(t-j\Delta t) \tag{5}$$

The replacement of dashpot elements with springpot ones introduces one more degree of freedom in the previously analyzed curves of conventional viscoelastic models: the order α of the derivative. In that sense, α governs the slope of the straight lines in the log-log representation of $|k^*|$ and LF. The adaptability introduced by this improvement has allowed the design of constitutive models, based on the triad of springs, dashpots, and springpots, that have shown the capability of simulating the viscoelastic behavior of many polymers and biomaterials [36].

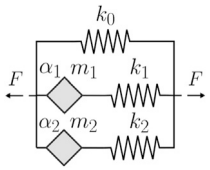

Fig. 6. Schematic representation of a fractional Maxwell-Wiechert model with two branches.

As stated in this brief review of the viscoelastic models, the most flexible one is the fractional Zener model. In that sense, it is necessary to design an algorithm to estimate the coefficients of each element of the fractional Zener model using the relaxation test. In order to extend the capability and flexibility of this algorithm to estimate different material behaviors, the constitutive equation used for this work is the Maxwell-Wiechert model with two branches, which is similar to the fractional Zener model but includes one more fractional Maxwell branch in parallel with the fractional Zener model (see Fig. 6). The algorithm simulated a fractional Zener model just introducing a null value in the k_2 and m_2 coefficients.

Equation (6) shows the constitutive equation of the fractional Maxwell-Wiechert model with two branches, and the estimation of this equation is included in Appendix A.

$$\begin{aligned}&\frac{m_1m_2}{k_1k_2}D^{\alpha_1+\alpha_2}[F]+\frac{m_1}{k_1}D^{\alpha_1}[F]+\frac{m_2}{k_2}D^{\alpha_2}[F]+F=\\&=\frac{m_1m_2}{k_1k_2}\left(k_0+k_1+k_2\right)D^{\alpha_1+\alpha_2}[\delta]+\frac{m_1}{k_1}\left(k_0+k_1\right)D^{\alpha_1}[\delta]+\\&+\frac{m_2}{k_2}\left(k_0+k_2\right)D^{\alpha_2}[\delta]+k_0\delta\end{aligned}\tag{6}$$

3. Numerical solution for the fractional Maxwell-Wiechert constitutive equation

As previously described, this investigation aims to use relaxation tests in RCBs to extrapolate their behavior at low to moderate frequencies under dynamic harmonic excitations. This extrapolation is made by estimating the coefficients of a fractional Zener model from the relaxation test and, after that, the obtained fractional Zener model is employed to simulate the response at low to moderate frequencies. The constitutive differential equation of the fractional Maxwell-Wiechert model with two branches (see Equation (6)) is solved numerically through the Grünwald-Letnikov method [33–35]. Since the purpose of this method is to execute a numerical approach, the Grünwald-Letnikov fractional derivative (see Equation (3)) is calculated by limiting the time discretization N to an integer value, thus leading to a specific step time Δt obtained from the division of total time used in the experimental relaxation test t_f by the time discretization N. Thus, the Grünwald-Letnikov fractional derivative is equal to the Equation (7), for a time $i\Delta t$ with i from 1 to N.

$$D^{\alpha}[f(i\Delta t)]=(\Delta t)^{-\alpha}\sum_{j=0}^{i-1}\left[\frac{\Gamma(j-\alpha)}{\Gamma(-\alpha)\Gamma(j+1)}f(\Delta t(i-j))\right]\tag{7}$$

In order to emulate an experimental relaxation test, a known and imposed displacement $\delta(t)$ is applied, and the output function $F(t)$ is unknown, except for the initial value $F(0)=0$. Equation (7) demonstrates that the fractional derivative is a so-called memory function because the fractional derivative of function f at time $i\Delta t$ is calculated by calling all previous steps of the function f. Therefore, the differential equation (6) can be solved explicitly starting from the initial value at the first time step, and generating an equation with a single unknown variable $F(\Delta t)$. Equation (8) shows the combination of equation (7) with the left side of equation (6) after the first time step ($i=1$). It shows that there is a single unknown variable, $F(\Delta t)$, on this side of the equation (6) at time step $i=1$. Taking into account that the right side of equation (6) only includes the known displacement data, the load $F(\Delta t)$ can be explicitly estimated.

$$\begin{aligned}&\frac{m_1m_2}{k_1k_2}D^{\alpha_1+\alpha_2}[F]+\frac{m_1}{k_1}D^{\alpha_1}[F]+\frac{m_2}{k_2}D^{\alpha_2}[F]+F=\\&=\left[\frac{m_1m_2}{k_1k_2}(\Delta t)^{-\alpha_1-\alpha_2}\left(F(i\Delta t)+\sum_{j=1}^{i-1}\left[\frac{\Gamma(j-\alpha_1-\alpha_2)}{\Gamma(-\alpha_1-\alpha_2)\Gamma(j+1)}F(\Delta t(i-j))\right]\right)\right]+\\&+\left[\frac{m_1}{k_1}(\Delta t)^{-\alpha_1}\left(F(i\Delta t)+\sum_{j=1}^{i-1}\left[\frac{\Gamma(j-\alpha_1)}{\Gamma(-\alpha_1)\Gamma(j+1)}F(\Delta t(i-j))\right]\right)\right]+\\&+\left[\frac{m_2}{k_2}(\Delta t)^{-\alpha_2}\left(F(i\Delta t)+\sum_{j=1}^{i-1}\left[\frac{\Gamma(j-\alpha_2)}{\Gamma(-\alpha_2)\Gamma(j+1)}F(\Delta t(i-j))\right]\right)\right]+F(i\Delta t)=\\&=\left[\frac{m_1m_2}{k_1k_2}(\Delta t)^{-\alpha_1-\alpha_2}+\frac{m_1}{k_1}(\Delta t)^{-\alpha_1}+\frac{m_2}{k_2}(\Delta t)^{-\alpha_2}+1\right]F(\Delta t)\end{aligned}\tag{8}$$

After this first step $i=1$, the combination of the equation (7) with the left side of the equation (6) gives the equation (9), where $F(i\Delta t)$ is the only unknown variable because $F(\Delta t(i-j))$ are the previous values which are estimated in a previous step. Thus, $F(i\Delta t)$ is calculated step by step until reach $i=N$.

$$\begin{aligned}&\frac{m_1m_2}{k_1k_2}D^{\alpha_1+\alpha_2}[F]+\frac{m_1}{k_1}D^{\alpha_1}[F]+\frac{m_2}{k_2}D^{\alpha_2}[F]+F=\\&=\left[\frac{m_1m_2}{k_1k_2}(\Delta t)^{-\alpha_1-\alpha_2}+\frac{m_1}{k_1}(\Delta t)^{-\alpha_1}+\frac{m_2}{k_2}(\Delta t)^{-\alpha_2}+1\right]F(i\Delta t)+\\&+\left[\frac{m_1m_2}{k_1k_2}(\Delta t)^{-\alpha_1-\alpha_2}\left(\sum_{j=1}^{i-1}\left[\frac{\Gamma(j-\alpha_1-\alpha_2)}{\Gamma(-\alpha_1-\alpha_2)\Gamma(j+1)}F(\Delta t(i-j))\right]\right)\right]+\\&+\left[\frac{m_1}{k_1}(\Delta t)^{-\alpha_1}\left(\sum_{j=1}^{i-1}\left[\frac{\Gamma(j-\alpha_1)}{\Gamma(-\alpha_1)\Gamma(j+1)}F(\Delta t(i-j))\right]\right)\right]+\\&+\left[\frac{m_2}{k_2}(\Delta t)^{-\alpha_2}\left(\sum_{j=1}^{i-1}\left[\frac{\Gamma(j-\alpha_2)}{\Gamma(-\alpha_2)\Gamma(j+1)}F(\Delta t(i-j))\right]\right)\right]\end{aligned}\tag{9}$$

The coefficients k_0, k_1, k_2, m_1, m_2, α_1, and α_2 are obtained from the best fitting of the numerically estimated $F_{num}(t)$ and the experimental $F_{exp}(t)$ registered during the relaxation test. The minimization of the mean squared error function (see Equation (10)) is the methodology used to reach this fitting. The algorithm is designed and implemented in Matlab® software.

$$\mathrm{MSE}=\frac{1}{N}\sum_{i=1}^{N}\left(F_{exp}^{(i)}-F_{num}^{(i)}\right)^2\tag{10}$$

This numerical procedure needs a sensibility analysis of the discretization N in order to guarantee a minimum error tolerance and, in that sense, the most critical point of this procedure is the use of the gamma function Γ in the calculation of the fractional derivatives of the constitutive equation (6). As an example of this statement, in a double-precision floating-point format (float64) the maximum value reached for the gamma function is $\Gamma(171)=7.2574\times10^{306}$. For higher values, variable precision must be increased. Thus, representing the rational function γ of Γ's contained in the summation of Equation (7) (see equation (11)) for different values of α and j, $\gamma(\alpha,j)$ function tends to 'NaN' result (Not a Number) after the critical value $j=171$, because $\Gamma(172)=\infty$ for float64 variables. In many coding languages, the use of the function $g(x)=\ln(\Gamma(x))$ increases this capability to very high values, changing the equation that represents $\gamma(\alpha,j)$ to the one included in Equation (12).

$$\gamma(\alpha,j)=\frac{\Gamma(j-\alpha)}{\Gamma(-\alpha)\Gamma(j+1)}\tag{11}$$

$$\gamma(\alpha,j)=\exp\{g(j-\alpha)-g(-\alpha)-g(j+1)\}\tag{12}$$

Fig. 7 represents a sensitivity analysis of $|k^*|$ and LF for a conventional Zener model with coefficients $k_0=1000$ N/mm, $k_1=1000$ N/mm, and $c_1=1000$ N.s/mm. First, the analytical solution of the constitutive equation for a conventional Zener model (see Fig. 4 for the equation of $|k^*|$ and LF versus frequency f) is represented with red

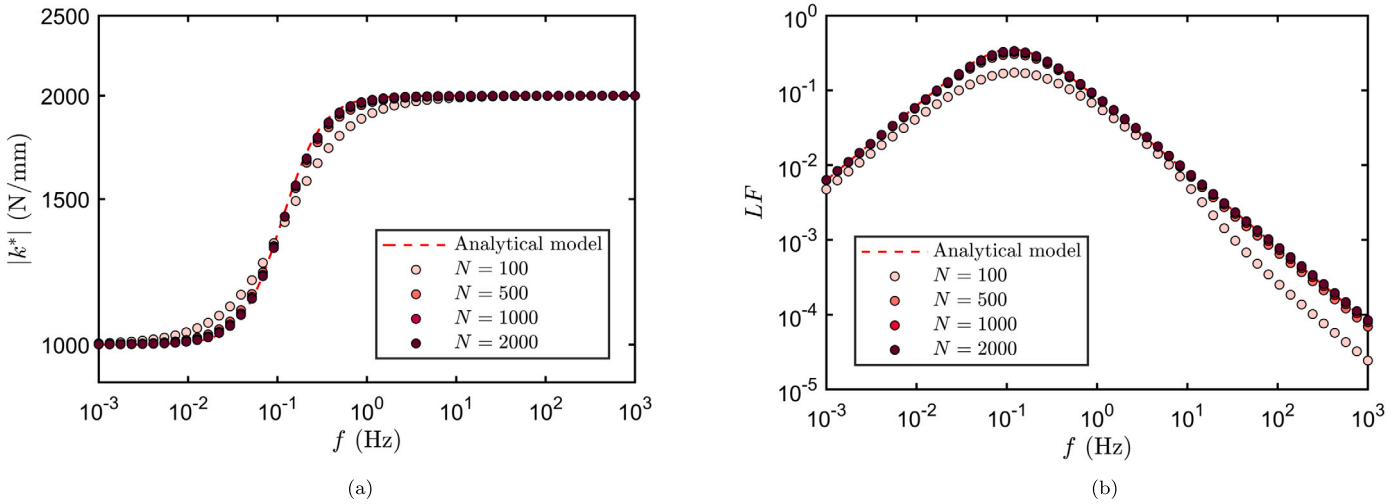

Fig. 7. Sensitivity analysis of time discretization N in a conventional Zener model ($k_0 = 1000$ N/mm; $k_1 = 1000$ N/mm; $c_1 = 1000$ N.s/mm) for (a) the absolute value of the dynamic stiffness, and (b) the loss factor.

dashed lines. Next, the constitutive equation is solved according to the Grünwald-Letnikov algorithm for the different values of the discretization N. Thus, the colored circles presented in Fig. 7 represent the approximation obtained from the algorithm for different values of the discretization N. For this analysis, the input function is a sinusoidal displacement $\delta(t) = e^{i2\pi ft}$ with a total time in order to reach 20 cycles in all the evaluated cases. The sense of this number of cycles is to reduce the influence of the initial transient behavior originated by the initial state $(\delta(0), F(0)) = (0, 0)$. The coefficients introduced in the algorithm are: $k_0 = 1000$ N/mm, $k_1 = 1000$ N/mm, $m_1 = 1000$ N.s/mm, $\alpha_1 = 1$, $k_2 = 0.001$ N/mm, and $m_2 = 0.001$ N.s/mm, and $\alpha_2 = 0$. Fig. 7 shows that a time discretization of 1000 steps per cycle is enough to reach satisfactory results, and the designed algorithm is also validated with this sensitivity analysis.

4. Experimental validation

As mentioned in the Introduction section, relaxation tests and dynamic harmonic tests are performed in RCBs to verify the capability of the fractional Zener model for the estimation of $|k^*|$ and LF in a range of 5 to 200 Hz (typical frequency range in combustion engines in the automotive sector) with a simple relaxation test. Three different RCBs manufactured by CMP Automotive company are used in this experimental validation (see Fig. 8a). These three cases are selected based on their range of stiffness and damping capability. Table 1 includes the geometry (see Fig. 1a for nomenclature identification) and rubber compound hardness. Bushing B1 is composed of a rubber compound with 25% natural rubber and a steel insert in the inner diameter. Bushing B2 shows a rubber compound with 50% natural rubber but it is manufactured with two steel inserts, covering the inner and outer diameters. Finally, bushing B3 is composed of a rubber compound with 50% natural rubber, steel inserts covering the inner and outer diameters, and a third steel insert located in the intermediate diameter. Relaxation tests are performed according to ISO3384 with a loading step of an imposed displacement of 0.5 mm in 6 s, and a relaxation step of 5 min. Dynamic harmonic tests are performed according to ISO4664 with a sinusoidal imposed displacement of amplitude $\delta_0 = 0.5$ mm and a frequency range from 5 to 200 Hz, except for the reference with the highest stiffness (ID B3) which is limited to a frequency range from 5 to 100 Hz. In all the references, the imposed displacement is applied radially. Both testing procedures are performed in a Schenck Series 56 servohydraulic testing machine. Fig. 8b shows the tool setup for the assembly of the rubber bushings in the testing machine. Rubber bushings are held along their outer and inner diameters in order to transmit the imposed displacement through the upper and lower arms of the testing machine. No preload loading step is applied to the bushings.

Table 1
Geometry and hardness of the evaluated rubber bushings.

ID	a (mm)	b (mm)	c (mm)	Shore A hardness
B1	38.0	12.1	62.0	70
B2	41.8	13.5	60.2	65
B3	41.1	11.0	42.0	60

Fig. 9 shows the registered load and the imposed displacement of relaxation tests for the RCBs, with three specimens for each part number or bushing. Each case is labeled with the ID Bx-SNy, where x represents the ID of each part number or bushing type and y identifies the serial number or individual specimen. Bushings are identified in a sequence based on their stiffness, with the softer bushing as ID B1 and the stiffest one as ID B3. B1 and B2 cases show dissimilar relaxation curves for each serial number, which is a common behavior within the manufacturing process variability of these rubber bushings. Fig. 10 shows the absolute value of the dynamic stiffness $|k^*|$ in graphs on the left (a, c, and e), and the loss factor LF on the right ones (b, d, and e), in their relation with frequency f. The graphs (a) and (b) in the first row represent data for bushing B1; plots (c) and (d) correspond to bushing B2; and plots (e) and (f) are for bushing B3. Markers identify the harmonic experimental tests: blue circles for SN1 tests, red quads for SN2 tests, and green diamonds for SN3 tests. Solid curves identify the frequency dependency of the estimated fractional Zener model whose parameters are obtained from the experimental relaxation test. The coefficients of these estimated fractional Zener models are included in Table 2, with the minimum mean square error (MSE) reached after each iterative process. In all the cases, the spring k_1 tends to the maximum value of the established upper limit ($k_1 = 10^7$ N/mm). Thus, the iterative process predicts in all cases a fractional Kelvin-Voigt model. Although the fractional Zener models approaches the experimental relaxation curves accurately, Fig. 10 shows that these specific models, extrapolated for higher frequencies, do not emulate the observed behavior of dynamic tests. Two possible reasons for this discrepancy are presented: (i) reason R1, the relaxation test does not have enough data to extrapolate accurately the bushing behavior at low to moderate frequencies; or (ii), reason R2, the selected viscoelastic model does not show the same behavior as the real rubber bushings for the strain rate range from relaxation tests (very low strain rate) to dynamic tests (low to moderate strain rates). Reason R1 is the most critical one because it

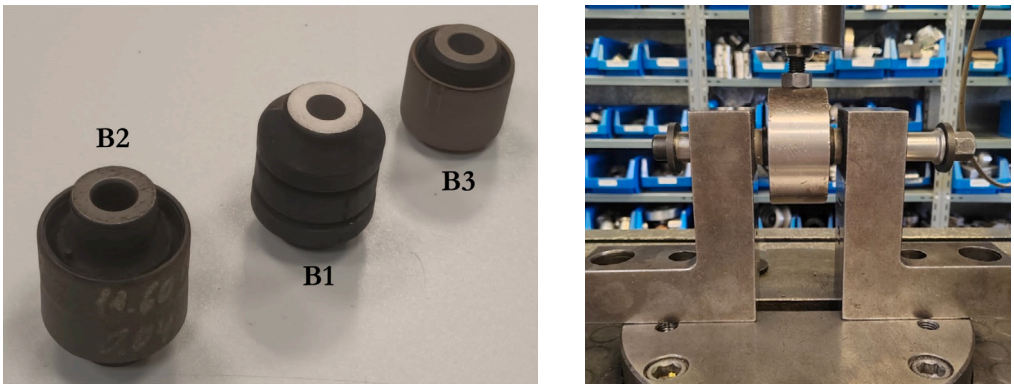

Fig. 8. (a) RCBs manufactured by CMP Automotive which are used in the experimental validation; (b) assembly of the rubber bushing in the servohydraulic testing machine.

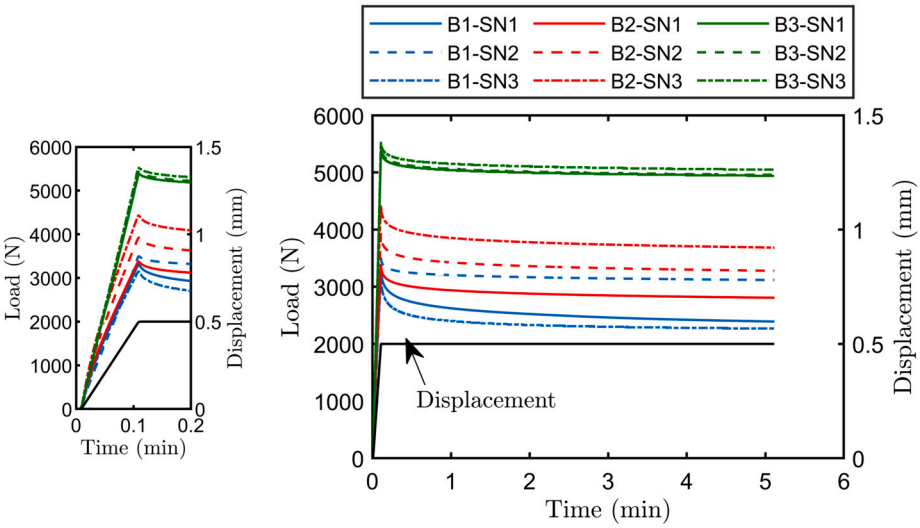

Fig. 9. Registered loads and displacement for the relaxation tests.

Table 2
Coefficients of the fractional Zener model obtained from the relaxation tests.

ID	k_0 (N/mm)	k_1 (N/mm)	m_1 (N.s$^\alpha$/mm)	α_1	MSE (N^2)
B1-SN1	2473.2	10^7	4594.1	0.107	23.0
B1-SN2	5694.6	10^7	1487.1	0.155	9.6
B1-SN3	4223.2	10^7	3718.2	0.373	1.0
B2-SN1	4794.4	10^7	2294.4	0.159	10.9
B2-SN2	5653.4	10^7	2562.0	0.160	13.2
B2-SN3	6352.5	10^7	2945.9	0.164	18.2
B3-SN1	9388.8	10^7	1719.7	0.191	5.4
B3-SN2	9369.1	10^7	1868.6	0.190	6.7
B3-SN3	9568.1	10^7	1835.2	0.192	7.2

would mean that the extrapolation procedure based on relaxation tests would estimate inaccurate properties.

A verification process is performed in order to demonstrate that the discrepancies presented in Fig. 10 are not due to reason R1 and the extrapolation procedure presented in this paper has enough data to determine the bushing behavior at low to moderate frequencies. The flow diagram presented in Fig. 11 shows the verification procedure steps. Firstly, the coefficients of a fractional Zener model are estimated from the experimental dynamic harmonic tests rather than from a relaxation test. Therefore, the algorithm of the MSE that must be minimized is modified. Equation (13) shows this new definition, where experimental $|k^*|$ and LF are the goals to be approached. The fractional Zener model estimated with this procedure is identified as Model 1. Displacement data from the experimental relaxation tests are used as input data in the algorithm to simulate the relaxation test with Model 1, obtaining the load response of this model. This load-displacement data represents the response of Model 1 under a relaxation test. The original algorithm with the MSE represented in equation (10) is used to estimate the coefficients of Model 2 using the load-displacement data obtained from Model 1. Dynamic harmonic tests are simulated with this new Model 2 in order to estimate the complex dynamic stiffness. After this procedure, the experimental complex dynamic stiffness is compared with the estimated ones.

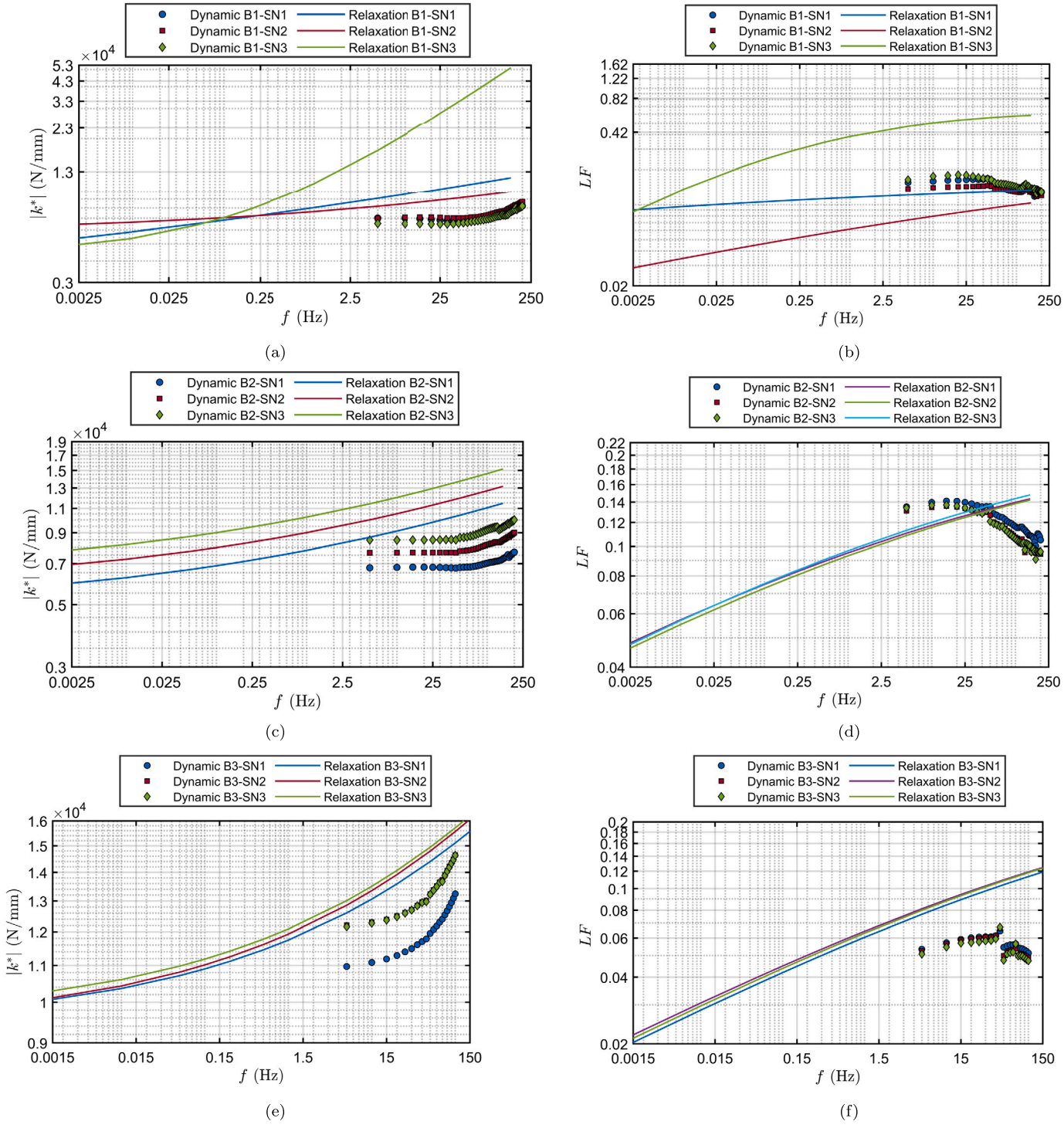

Fig. 10. Absolute value of the dynamic stiffness (a, c, and e) and loss factor (b, d, and f), for bushing 1 (a and b), bushing 2 (c and d), and bushing 3 (e and f). Data included in the graphs: (i) the experimental dynamic tests of the RCBs, identified with markers, each one for each serial number (blue circles for SN1, red quads for SN2, and green diamonds for SN3); and (ii), estimated fractional Zener model from the relaxation tests, identified with solid curves.

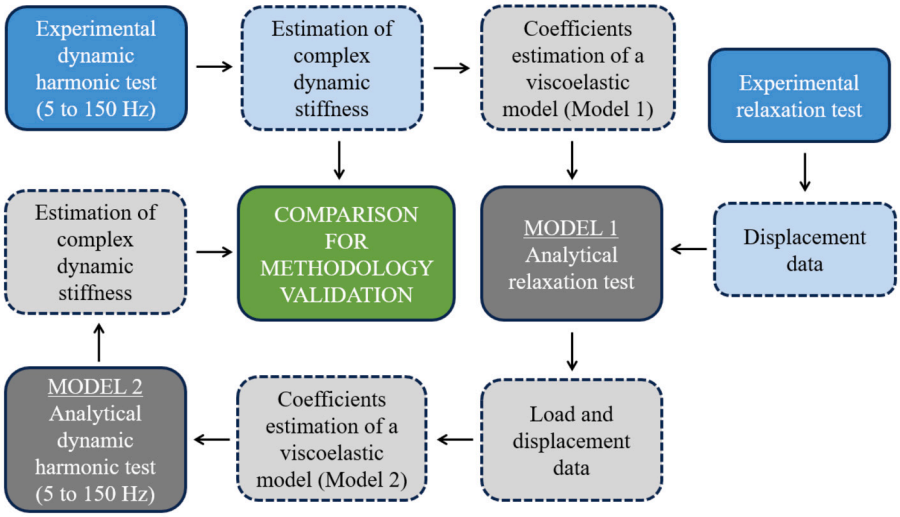

Fig. 11. Flow diagram used to verify the capability of the relaxation test to extrapolate the low-to-moderate frequency behavior of a viscoelastic material.

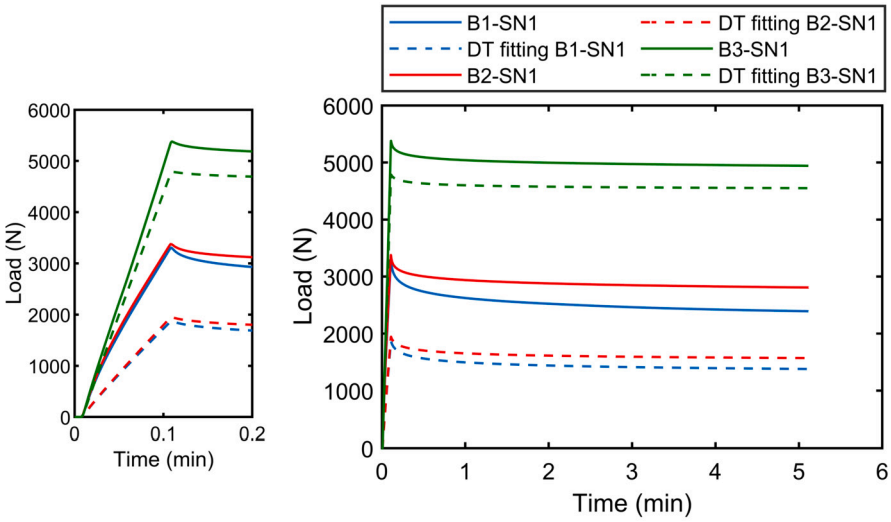

Fig. 12. Registered loads of the relaxation tests of SN1 cases in comparison with the relaxation curves of the estimated Zener models from the dynamic experimental tests.

To conclude, the main purpose of this procedure is to generate a new viscoelastic Model 2 based on analytical relaxation data created with Model 1, and then calculate a new dynamic stiffness from Model 2. If a relaxation test did not have sufficient data to estimate the frequency response, the new dynamic stiffness generated with Model 2 should exhibit mismatches with the experimental dynamic stiffness. This would indicate that some data is lost in the extrapolation process. In contrast, if both stiffnesses are similar, it would mean that relaxation tests have sufficient data to apply accurately an extrapolation procedure to estimate the low-to-moderate frequency behavior of viscoelastic materials.

In Fig. 12 the relaxation load curves estimated by Model 1 are represented by dashed lines and the load curves of the experimental relaxation tests are indicated by solid lines. The response of Model 1 shows lower stiffness than that from the experimental relaxation tests. These significant differences verify that standard commercial rubber bushings show a frequency dependency of the dynamic stiffness dissimilar to a fractional Zener model behavior when the model is used to simulate behaviors from very small deformation rates (relaxation tests) to typical dynamic frequencies with high deformation rates (10 to 150 Hz). Thus, reason R2, which was established previously, is verified.

Fig. 13 shows the comparison between experimental $|k^*|$ and LF data and the estimated curves with Model 2. Thus, leading to a very good fitting of both properties corresponding to the three bushings. Therefore, the relaxation curves contained enough information to estimate the low to moderate frequency response, and the reason R1, which was previously stated, was refuted. The main difficulty is to establish an analytical viscoelastic model that accurately follows the behavior of real materials from very small deformation rates (relaxation tests) to higher deformation rates (harmonic dynamic tests).

$$\mathrm{MSE} = \frac{1}{n}\sum_{i=1}^{n}\left[\left(\frac{LS_{exp}^{(i)} - LS_{num}^{(i)}}{LS_{exp}^{(i)}}\right)^2 + \left(\frac{|k^*|_{exp}^{(i)} - |k^*|_{num}^{(i)}}{|k^*|_{exp}^{(i)}}\right)^2\right] \tag{13}$$

5. Conclusions

The aim of this research is to analyze the capability of a relaxation test to estimate the frequency response of standard rubber bushings. An extrapolation procedure is designed to reach this goal. Firstly, the parameters of a fractional Zener model are estimated from an experimen-

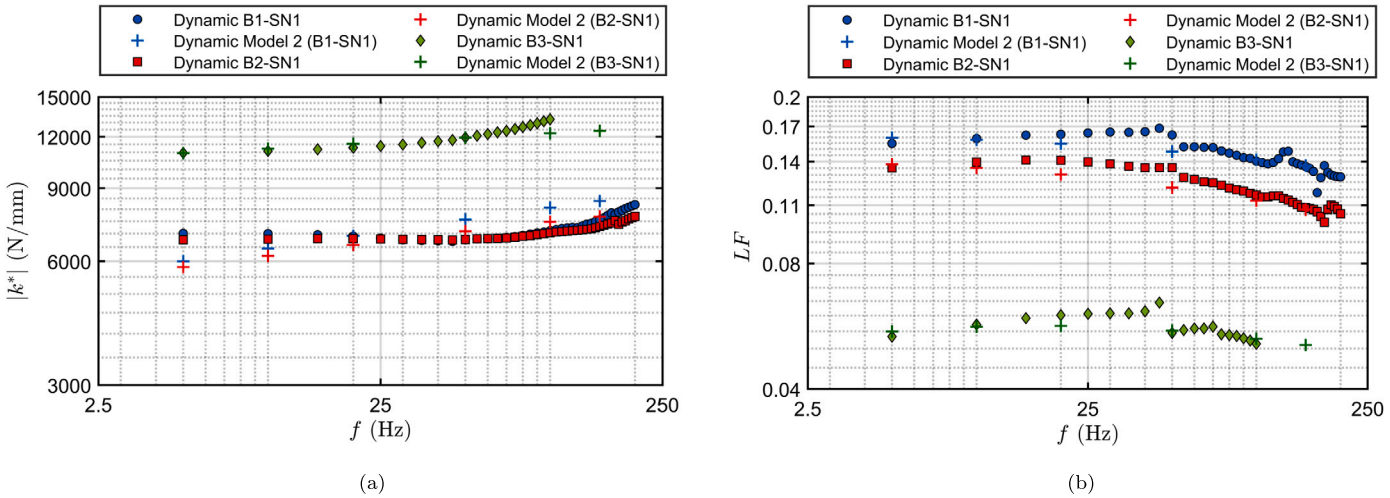

Fig. 13. Comparison of the experimental dynamic response of rubber bushings and the dynamic simulation with Model 2; (a) $|k^*|$ and, (b) LF.

tal relaxation test. Next, the dynamic stiffness in a frequency range from 5 to 150 Hz is predicted with this fractional Zener model, and results are compared to those obtained experimentally in a servo-hydraulic testing machine. This investigation has generated the next conclusions:

i. The fractional Zener model does not show the capability to follow the real behavior of rubber bushings from very low strain rates (typical of a relaxation test) to low-to-moderate strain rates (dynamic harmonic test).
ii. Relaxation tests have enough data to extrapolate accurately the frequency response of a viscoelastic material.
iii. The extrapolation process to estimate the frequency response of rubber bushings with relaxation tests needs to explore and design analytical viscoelastic models that show the capability to simulate the real behavior of rubber bushings from very low strains to moderate strains.
iv. The influence of dependence on the amplitude presented by certain elastomers, especially those with carbon fibers (Payne effect), could affect the extrapolation process because, in each cycle of a dynamic harmonic test, a sweep of strain is carried out until reaching the peak amplitudes. However, the relaxation tests subject the bushing to the highest value of strain the most of the testing time.

These conclusion remarks open future research related to the next points:

i. Design of novel viscoelastic models that follow a similar behavior of standard rubber bushings for frequency ranges from very low values, with similar deformation rates of a relaxation test, to moderate values, such as higher frequencies of combustion engines. The use of these analytical models would allow the application of the extrapolation procedure to estimate the frequency response with a simple relaxation test.
ii. Analyzing the influence of Payne effect in the extrapolation procedure defined in this investigation.
iii. Extend the extrapolation procedure to higher frequencies, using low-to-moderate frequency dynamic harmonic tests to estimate the high-frequency response.

CRediT authorship contribution statement

Jose Calaf-Chica: Conceptualization, Methodology, Supervision, Writing – original draft. **Víctor Cea-González:** Formal analysis, Investigation, Resources. **María-José García-Tárrago:** Conceptualization, Methodology, Writing – review & editing. **Francisco-Javier Gómez-Gil:** Conceptualization, Methodology, Writing – review & editing.

Declaration of competing interest

The authors declare that they have no known competing financial interests or personal relationships that could have appeared to influence the work reported in this paper.

Data availability

Data will be made available on request.

Acknowledgements

The authors greatly acknowledge the collaboration of CMP Automotive in the selection and experimental testing procedures of the rubber bushings.

Appendix A. Constitutive equation of the fractional Maxwell-Wiechert model

Fig. 6 shows a schematic view of the fractional Maxwell-Wiechert viscoelastic model, composed of an elastic spring in parallel with two fractional Maxwell branches. The displacement is identified with δ and the displacement of each element included in the Maxwell branches is identified as: δ_{1k} and δ_{2k}, for the displacements of each spring; and, δ_{1m} and δ_{2m}, for the displacements of each springpot. The total load F is divided at each branch in the next contributions: F_0 for the branch with the single spring, F_1 for the Maxwell branch identified as number 1, and F_2 for the Maxwell branch number 2.

The total displacement δ is equal to the contribution of each element of each branch. Applying a fractional derivative gives the relation included in equation (A.1).

$$\left.\begin{aligned}\delta &= \delta_{1k} + \delta_{1m}\\ \delta &= \delta_{2k} + \delta_{2m}\end{aligned}\right\} \rightarrow \left\{\begin{aligned}D^{\alpha_1}\delta &= D^{\alpha_1}\delta_{1k} + D^{\alpha_1}\delta_{1m}\\ D^{\alpha_2}\delta &= D^{\alpha_2}\delta_{2k} + D^{\alpha_2}\delta_{2m}\end{aligned}\right. \tag{A.1}$$

The load F_i of each Maxwell branch i is related to the displacement of each elastic spring and each springpot by basic constitutive equations. From these equations, the fractional derivatives of the displacement of each element are related to the load of each branch (see equation (A.2)).

$$F_1 = k_1\delta_{1k} \rightarrow D^{\alpha_1}\delta_{1k} = \frac{1}{k_1}D^{\alpha_1}F_1 \qquad D^{\alpha_1}\delta_{1m} = \frac{F_1}{m_1} \tag{A.2}$$

Equation (A.3) is obtained applying the equation (A.2) into the equation (A.1).

$$\left.\begin{array}{l} D^{\alpha_1}\delta = D^{\alpha_1}\delta_{1k} + D^{\alpha_1}\delta_{1m} \\ D^{\alpha_2}\delta = D^{\alpha_2}\delta_{2k} + D^{\alpha_2}\delta_{2m} \end{array}\right\} \rightarrow \left\{\begin{array}{l} D^{\alpha_1}\delta = \frac{1}{k_1}D^{\alpha_1}F_1 + \frac{F_1}{m_1} \\ D^{\alpha_2}\delta = \frac{1}{k_2}D^{\alpha_2}F_2 + \frac{F_2}{m_2} \end{array}\right. \tag{A.3}$$

The application of the Laplace transform to equation (A.3) estimates the equation (A.4).

$$s^{\alpha_1}\mathcal{L}[\delta] = \frac{s^{\alpha_1}}{k_1}\mathcal{L}\left[F_1\right] + \frac{1}{m_1}\mathcal{L}\left[F_1\right] \rightarrow \mathcal{L}\left[F_1\right] = \frac{s^{\alpha_1}}{\frac{s^{\alpha_1}}{k_1}+\frac{1}{m_1}}\mathcal{L}[\delta] = \frac{k_1 m_1 s^{\alpha_1}}{m_1 s^{\alpha_1}+k_1}\mathcal{L}[\delta] \tag{A.4}$$

Laplace transform is also applied to: (i) the relation of the total load F with the load at each branch; and (ii), the relation between the load F_0 of the branch 0, which includes the single elastic spring, and the displacement δ_0 of this branch 0 (see equation (A.5)).

$$F = F_0 + F_1 + F_2 \rightarrow \mathcal{L}[F] = \mathcal{L}\left[F_0\right] + \mathcal{L}\left[F_1\right] + \mathcal{L}\left[F_2\right] \qquad F_0 = k_0\delta \rightarrow \mathcal{L}\left[F_0\right] = k_0\mathcal{L}[\delta] \tag{A.5}$$

Equation (A.6) is obtained combining equations (A.4) and (A.5).

$$\mathcal{L}[F] = k_0\mathcal{L}[\delta] + \frac{k_1 m_1 s^{\alpha_1}}{m_1 s^{\alpha_1}+k_1}\mathcal{L}[\delta] + \frac{k_2 m_2 s^{\alpha_2}}{m_2 s^{\alpha_2}+k_2}\mathcal{L}[\delta] \tag{A.6}$$

Equation (A.7) is obtained with basic algebraic operations in equation (A.6).

$$\begin{aligned} &m_1 m_2 s^{\alpha_1+\alpha_2}\mathcal{L}[F] + m_1 k_2 s^{\alpha_1}\mathcal{L}[F] + m_2 k_1 s^{\alpha_2}\mathcal{L}[F] + k_1 k_2\mathcal{L}[F] = \\ &= m_1 m_2\left(k_0+k_1+k_2\right)s^{\alpha_1+\alpha_2}\mathcal{L}[\delta] + k_2 m_1\left(k_0+k_1\right)s^{\alpha_1}\mathcal{L}[\delta] + \\ &\quad + k_1 m_2\left(k_0+k_2\right)s^{\alpha_2}\mathcal{L}[\delta] + k_0 k_1 k_2\mathcal{L}[\delta] \end{aligned} \tag{A.7}$$

The application of the inverse Laplace transform to equation (A.7) gives the constitutive equation of the fractional Maxwell-Wiechert model with two branches (see equation (A.8)).

$$\begin{aligned} &\frac{m_1 m_2}{k_1 k_2}D^{\alpha_1+\alpha_2}[F] + \frac{m_1}{k_1}D^{\alpha_1}[F] + \frac{m_2}{k_2}D^{\alpha_2}[F] + F = \\ &= \frac{m_1 m_2}{k_1 k_2}\left(k_0+k_1+k_2\right)D^{\alpha_1+\alpha_2}[\delta] + \frac{m_1}{k_1}\left(k_0+k_1\right)D^{\alpha_1}[\delta] + \\ &\quad + \frac{m_2}{k_2}\left(k_0+k_2\right)D^{\alpha_2}[\delta] + k_0\delta \end{aligned} \tag{A.8}$$

References

[1] J. Kumar, G. Bhushan, Modelling of a semi-active vibration absorber featuring variable stiffness and variable damping using magnetorheological materials, Mater. Today Proc. (2023), https://doi.org/10.1016/J.MATPR.2023.04.005.

[2] A. Belhocine, N.M. Ghazaly, Effects of material properties on generation of brake squeal noise using finite element method, Lat. Am. J. Solids Struct. 12 (2015) 1432–1447, https://doi.org/10.1590/1679-78251520.

[3] A. Belhocine, N.M. Ghazaly, Effects of young's modulus on disc brake squeal using finite element analysis, Int. J. Acoust. Vib. 21 (2016) 292–300, https://doi.org/10.20855/IJAV.2016.21.3423.

[4] N. Stojanovic, A. Belhocine, O.I. Abdullah, I. Grujic, The influence of the brake pad construction on noise formation, people's health and reduction measures, Environ. Sci. Pollut. Res. 30 (2023) 15352–15363, https://doi.org/10.1007/S11356-022-23291-3/METRICS.

[5] S.M.A. Akmal, G. Bharathiraja, Analysis of engine mount material for automotive vibration and noise reduction, Mater. Today Proc. 62 (2022) 2235–2239, https://doi.org/10.1016/J.MATPR.2022.03.462.

[6] C. Wang, Sound transmission loss of an automotive floor panel section with cross members, Appl. Acoust. 202 (2023) 109177, https://doi.org/10.1016/J.APACOUST.2022.109177.

[7] P. Arnold, S. Kirsch, M.R. Kirchhoff, R. Hanke-Rauschenbach, Startup optimization of an automotive polymer electrolyte membrane fuel cell system with dynamic hydrogen reference electrodes, J. Power Sources 558 (2023) 232604, https://doi.org/10.1016/J.JPOWSOUR.2022.232604.

[8] A. Cernat, C. Pana, N. Negurescu, C. Nutu, D. Fuiorescu, G. Lazaroiu, Aspects of an experimental study of hydrogen use at automotive diesel engine, Heliyon 9 (2023) e13889, https://doi.org/10.1016/J.HELIYON.2023.E13889.

[9] F.E.B. Feitosa, A.L. Costa, Application of a multicriteria methodology for evaluation of energy alternatives for hydrogen production for the automotive sector – case study, Int. J. Hydrog. Energy 46 (2021) 20799–20814, https://doi.org/10.1016/J.IJHYDENE.2021.03.209.

[10] H.T. Arat, Recycling and reusing batteries: a significant way for effective sustainability of fcevs and evs, Int. J. Hydrog. Energy (2023), https://doi.org/10.1016/J.IJHYDENE.2023.01.189.

[11] X. Hua, A. Thomas, K. Shultis, Recent progress in battery electric vehicle noise, vibration, and harshness, Sci. Progr. 104 (3 2021), https://doi.org/10.1177/00368504211005224/.

[12] T. Gejguš, J. Schröder, K. Loos, A. Lion, M. Johlitz, Advanced characterisation of soft polymers under cyclic loading in context of engine mounts, Polymers 14 (2022) 429, https://doi.org/10.3390/POLYM14030429.

[13] M. Schnell, M. Gradtke, F. Gauterin, Fixture for high-frequency viscoelastic transfer path analysis in application to elastomer sealing rings in electric motors, Vibration 4 (2021) 414–421, https://doi.org/10.3390/VIBRATION4020027.

[14] Y. Du, R.A. Burdisso, E. Nikolaidis, D. Tiwari, Effects of isolators internal resonances on force transmissibility and radiated noise, J. Sound Vib. 268 (2003) 751–778, https://doi.org/10.1016/S0022-460X(03)00036-1.

[15] Öner Murat Akbaba, B. Yıldırım, G. Canbaloğlu, Vibration based fatigue analysis of a structure integrated on an air vehicle by using experimental and theoretical methods, Results Eng. 15 (2022) 100549, https://doi.org/10.1016/J.RINENG.2022.100549.

[16] M.J.G. Tárrago, L. Kari, J. Vinolas, N. Gil-Negrete, Frequency and amplitude dependence of the axial and radial stiffness of carbon-black filled rubber bushings, Polym. Test. 26 (2007) 629–638, https://doi.org/10.1016/J.POLYMERTESTING.2007.03.011.

[17] S. Cyril, H. Manikandan, Optimization of engine and transmission mounting system for a v6 front wheel drive vehicle, Mater. Today Proc. 72 (2023) 2564–2568, https://doi.org/10.1016/J.MATPR.2022.10.028.

[18] J. Kemna, J. Edelmann, M. Plöchl, Influences on long-term behaviour of elastomer chassis bushings considering their geometric design and rubber compounds, Polym. Test. 65 (2018) 69–77, https://doi.org/10.1016/J.POLYMERTESTING.2017.11.001.

[19] M.S. Qatu, Recent research on vehicle noise and vibration, Int. J. Veh. Noise Vib. 8 (2012) 289–301, https://doi.org/10.1504/IJVNV.2012.051536.

[20] B. Yoon, J.Y. Kim, U. Hong, M.K. Oh, M. Kim, S.B. Han, J.D. Nam, J. Suhr, Dynamic viscoelasticity of silica-filled styrene-butadiene rubber/polybutadiene rubber (sbr/br) elastomer composites, Composites, Part B, Eng. 187 (2020) 107865, https://doi.org/10.1016/J.COMPOSITESB.2020.107865.

[21] K. Junik, G. Lesiuk, M. Barcikowski, W. Błażejewski, A. Niemiec, M. Grobelny, K. Otczyk, J.A.F.O. Correia, Impact of the hardness on the selected mechanical properties of rigid polyurethane elastomers commonly used in suspension systems, Eng. Fail. Anal. 121 (2021) 105201, https://doi.org/10.1016/J.ENGFAILANAL.2020.105201.

[22] A. Erenchun, B. Blanco, N. Gil-Negrete, B. Wang, L. Kari, Effect of lubrication on the mechanical behavior of magnetorheological elastomers in compression mode, Polym. Test. 111 (2022) 107617, https://doi.org/10.1016/J.POLYMERTESTING.2022.107617.

[23] X.Q. Zhou, D.Y. Yu, X.Y. Shao, S.Q. Zhang, S. Wang, Research and applications of viscoelastic vibration damping materials: a review, Compos. Struct. 136 (2016) 460–480, https://doi.org/10.1016/J.COMPSTRUCT.2015.10.014.

[24] W.D. Kim, S. Hur, C.S. Woo, W.S. Kim, S.B. Lee, A study of the static and dynamic characteristics for automotive rubber mount by fea and experiment, Key Eng. Mater. 297–300 (2005) 299–304, https://doi.org/10.4028/WWW.SCIENTIFIC.NET/KEM.297-300.299.

[25] R.P. Chartoff, J.D. Menczel, S.H. Dillman, Dynamic mechanical analysis (dma), in: Thermal Analysis of Polymers: Fundamentals and Applications, 2008, pp. 387–495.

[26] L.E. Ooi, Z.M. Ripin, Dynamic stiffness and loss factor measurement of engine rubber mount by impact test, Mater. Des. 32 (2011) 1880–1887, https://doi.org/10.1016/J.MATDES.2010.12.015.

[27] E.E. Ungar, E.M. Kerwin, Loss factors of viscoelastic systems in terms of energy concepts, J. Acoust. Soc. Am. 34 (1962) 954–957, https://doi.org/10.1121/1.1918227.

[28] A. Bonfanti, J.L. Kaplan, G. Charras, A. Kabla, Fractional viscoelastic models for power-law materials, Soft Matter 16 (2020) 6002–6020, https://doi.org/10.1039/D0SM00354A.

[29] B. Babaei, A. Davarian, K.M. Pryse, E.L. Elson, G.M. Genin, Efficient and optimized identification of generalized maxwell viscoelastic relaxation spectra, J. Mech. Behav. Biomed. Mater. 55 (2016) 32–41, https://doi.org/10.1016/j.jmbbm.2015.10.008.

[30] M.V. Shitikova, V.V. Kandu, A.I. Krusser, On nonlinear vibrations of an elastic plate on a fractional viscoelastic foundation in a viscoelastic medium in the presence of the one-to-one internal resonance, J. Sound Vib. 549 (2023) 117564, https://doi.org/10.1016/J.JSV.2023.117564.

[31] J. Freundlich, Transient vibrations of a fractional kelvin-voigt viscoelastic cantilever beam with a tip mass and subjected to a base excitation, J. Sound Vib. 438 (2019) 99–115, https://doi.org/10.1016/J.JSV.2018.09.006.

[32] S. Paunović, M. Cajić, D. Karličić, M. Mijalković, A novel approach for vibration analysis of fractional viscoelastic beams with attached masses and base excitation, J. Sound Vib. 463 (2019) 114955, https://doi.org/10.1016/J.JSV.2019.114955.

[33] R. Scherer, S.L. Kalla, Y. Tang, J. Huang, The grünwald–letnikov method for fractional differential equations, Comput. Math. Appl. 62 (2011) 902–917, https://doi.org/10.1016/J.CAMWA.2011.03.054.

[34] A. Dabiri, E.A. Butcher, M. Nazari, Coefficient of restitution in fractional viscoelastic compliant impacts using fractional chebyshev collocation, J. Sound Vib. 388 (2017) 230–244, https://doi.org/10.1016/J.JSV.2016.10.013.

[35] P.R.N. Tuwa, T. Molla, S. Noubissie, S.T. Kingni, K. Rajagopal, Analysis of a quarter car suspension based on a kelvin–voigt viscoelastic model with fractional-order derivative, Int. J. Non-Linear Mech. 137 (2021) 103818, https://doi.org/10.1016/J.IJNONLINMEC.2021.103818.

[36] M. Sasso, G. Palmieri, D. Amodio, Application of fractional derivative models in linear viscoelastic problems, Mech. Time-Depend. Mater. 15 (2011) 367–387, https://doi.org/10.1007/S11043-011-9153-X/METRICS.